Nonlinear Finite Element Analysis and Fatigue Damage Assessment of Wind-Induced Vibration for the Tension Cable-Supported Power Transmission Structure

Jingyang Li , Bangjie Wang , Tao Wang * , Zhengliang Li

Posted Date: 25 September 2023

doi: 10.20944/preprints202309.1650.v1

Keywords: Tension cable-supported power transmission structure; Wind-induced vibration; Nonlinear finite element; Wind-induced fatigue damage

Article

Nonlinear Finite Element Analysis and Fatigue Damage Assessment of Wind-Induced Vibration for the Tension Cable-Supported Power Transmission Structure

Jingyang Li [1], Bangjie Wang [1], Tao Wang [2,3,*] and Zhengliang Li [1,4]

[1] School of Civil Engineering, Chongqing University, Chongqing, 40045, China; jingyanglisc@163.com; bangjiewang@cqu.edu.cn; lizhengl@hotmail.com
[2] School of Transportation Science and Engineering, Harbin Institute of Technology, Harbin, Heilongjiang, China, 150040; taowang@alu.cqu.edu.cn
[3] Chongqing Research Institute of Harbin Institute of Technology, Harbin Institute of Technology, Chongqing, China, 401151
[4] Chongqing Key Laboratory of Wind Engineering and Wind Resources Utilization, Chongqing 400045, China
* Correspondence: taowang@alu.cqu.edu.cn

Abstract: The tension cable-supported power transmission structure (TC-PTS) is a new type of power transmission structure suitable for mountainous terrain, which is sensitive to wind load. In this regard, a nonlinear finite element analysis model of wind-induced vibration is proposed for the TC-PTS, and the wind-induced vibration response of the structure is analyzed. Firstly, the tangent stiffness matrix of the three-dimensional truss element for the supporting suspension cable and transmission line, considering the geometric nonlinearity of structures, is derived through the relationship between the element elastic energy and its displacement. Subsequently, the element mass matrix and damping matrix of the supporting suspension cable and transmission line, as well as the element nodal load vector obtained from wind load equivalence are given. Then, based on the nonlinear finite element theory, the nonlinear dynamic equation of wind-induced vibration is established for the TC-PTS and solved by Newmark-β method combined with Newton-Raphson iterative method. Furthermore, the rain-flow counting method and Miner's linear fatigue cumulative damage theory were used for wind induced fatigue damage assessment. Finally, a two-span TC-PTS is selected as an example, and the wind-induced nonlinear vibration and fatigue damage assessment are analyzed through the proposed model. The results show that the proposed model has high computational accuracy and efficiency. With the increase of wind speed and wind direction angle, the maximum lateral displacement and tension of the supporting suspension cable and transmission line increase, and their degree of increase shows a nonlinear trend. In terms of the wind-induced fatigue analysis results of TC-PTS, the fatigue damage at the end of the supporting-conductor suspension cable is greater than the fatigue damage at its midpoint. Compared to the fatigue damage at the midpoint of the conductor, the fatigue damage at the end of the conductor is less affected by wind direction angle, and both are more significantly affected by the wind speed.

Keywords: tension cable-supported power transmission structure; wind-induced vibration; nonlinear finite element; wind-induced fatigue damage

1. Introduction

As an electric energy infrastructure, a high-voltage transmission tower-line system is an important part of the transmission and distribution systems in the power grid [1]. With the boom in the development of power grid construction, the number of power transmission structures erected in mountainous terrains has been increasing [2]. However, the paths required for transmission line

Preprints (www.preprints.org) | NOT PEER-REVIEWED | Posted: 25 September 2023 doi:10.20944/preprints202309.1650.v1

corridors in mountainous areas are becoming tighter, and the selection of tower locations is becoming increasingly difficult. For example, the transmission tower-line system in the Guangxi karst terrain, Xinjiang Danxia terrain, and other special complex mountainous terrain alignments and tower positions owing to terrain restrictions are often difficult to set up, resulting in a wide range of line rerouting.

Therefore, the electric power industry in recent years began to explore new power transmission structures suitable for mountainous areas, the tension cable-supported power transmission structure (TC-PTS) is one of the new overhead power transmission structure. The TC-PTS primarily consists of a conductor, ground wire, supporting-conductor suspension cable, supporting-ground wire suspension cable, tension-resistant insulator strings, and fixed brackets. The structural schematics are illustrated in Figure 1. Among them, the supporting suspension cable made of high-strength steel strands is the main load-bearing structure, which is usually fixed in mountain rock or rigid fixed brackets, the transmission line through the connection of fittings, and the supporting suspension cable to form a coupling system.

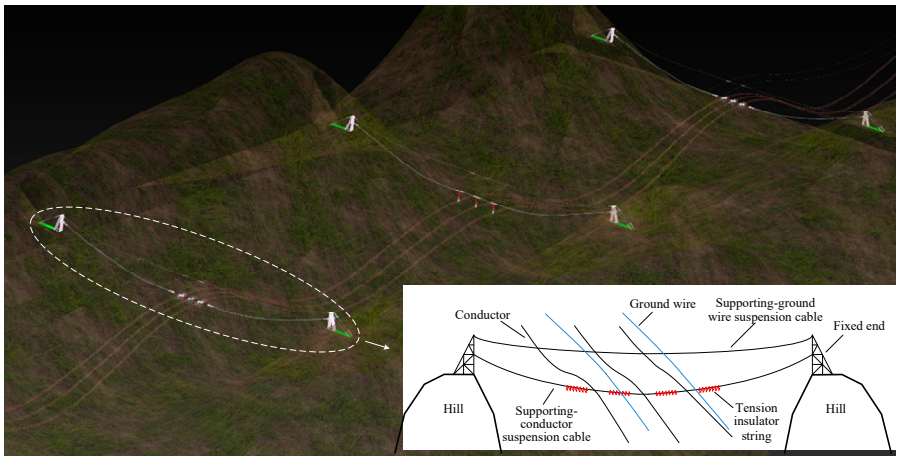

Figure 1. Schematic diagram of the tension cable-supported power transmission structure.

The supporting suspension cables and transmission lines in TC-PTS are large-span, highly flexible spatial suspension structures, which are typical wind-sensitive structures. In addition, the structure has mechanical characteristics such as large deformation and small strain, and the geometric nonlinear effect is significant. Compared with the transmission line and transmission tower-line systems, the transmission line of the TC-PTS forms a coupled system with supporting suspension cables, and its geometric nonlinear effect is more significant. Scholars have conducted a series of studies to address the wind-induced nonlinear vibration problem of transmission lines and transmission tower line systems. In early studies, transmission lines were usually considered as suspension structures; and their static and dynamic characteristics are analyzed [3–5]. With the development of the finite element method and large deformation theory, the wind-induced vibration analysis of transmission lines and tower-line systems is generally performed using a nonlinear finite element method. The mechanical model of the transmission line and tower-line system based on the truss element is convenient for performing various types of wind vibration and other static and dynamic analysis [6,7]. The mechanical model of the transmission line and tower-line system established by using a cable element and beam element can consider the torsional and bending capacity of the transmission line and then study complex wind vibration problems such as galloping [8–11]. Scholars have analyzed the dynamic models of transmission lines and tower-line systems and their wind-induced nonlinear vibration problems in detail through theoretical studies and numerical simulations, and have achieved significant research results. However, nonlinear dynamic modeling and wind-induced vibration analyses of TC-PTS have rarely been reported.

To this end, this study establishes a finite element model of TC-PTS based on 3D truss elements, then the nonlinear dynamic equations of the structure are formed, and the iterative solution process of the Newmark-β method combined with the Newton–Raphson method is provided. In addition,

Preprints (www.preprints.org) | NOT PEER-REVIEWED | Posted: 25 September 2023 doi:10.20944/preprints202309.1650.v1

wind vibration fatigue assessment was performed by combining the rainfall counting method with the Miner linear fatigue cumulative damage theory. The remainder of this paper is organized as follows. Section 2 exhibits the simplified mechanical model of TC-PTS. The nonlinear finite element equation of wind-induced vibration and fatigue damage assessment method for TC-PTS are shown in Section 3. Subsequently, Section 4 provides an example and the corresponding discussion. Finally, some conclusions are summarized in Section 5.

2. Simplified mechanical model of TC-PTS

2.1. Structural parameters and boundary conditions

The simplified model and the structural parameters of the TC-PTS are shown in Figure 2. l_s is the horizontal distance between the ends on both sides of the same suspension cable, l_c is the horizontal distance between two adjacent spans of the suspension cable, h_s is the height difference between the ends of both sides of the same suspension cable, h_c is the height difference between the positions of the same span of the conductor or ground wire in the adjacent hanging points of the suspension cable, h_{wg} is the height difference between the ends of the supporting-ground wire suspension cable and the corresponding ends of the supporting-conductor suspension cable.

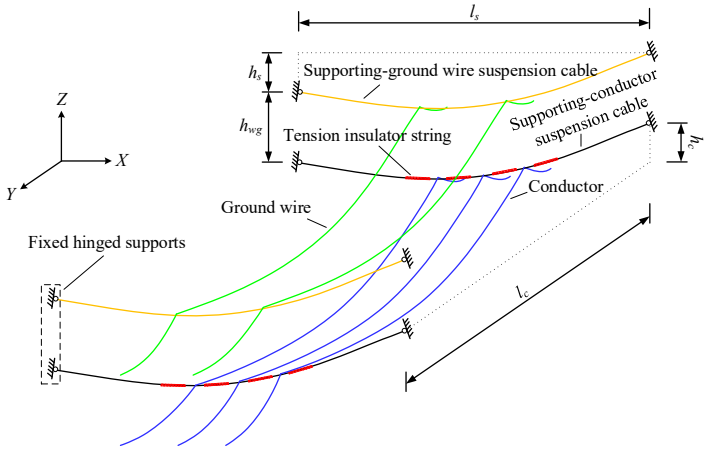

Figure 2. Simplified model and structural parameters of the tension cable-supported power transmission structure.

The connections between the ends of the supporting suspension cables, fixed supports, and the connection between the transmission lines and corresponding suspension cables at the boundaries are hinged. Therefore, all the supports at the TC-PTS boundary can be considered as fixed hinged supports.

2.2. Initial shape of TC-PTS

To establish a finite element model of the TC-PTS that considers the geometric nonlinear effect, it is necessary to first obtain the initial shape and initial internal force under gravity loading. For the supporting suspension cables and transmission lines of the TC-PTS, its initial shape can be simplified as a parabolic model, and the functional expression required to establish this parabolic model is

$$y = 4xf_m\left(1 - x/l\right)/l \tag{1}$$

where y is the vertical distance from the calculation point to the starting point, x is the horizontal distance from the calculation point to the starting point, l is the horizontal distance from the end point to the starting point, and f_m is the spanning mid-arc droop calculated according to Eq. (2):

$$f_m = ql^2/(8\sigma_0\cos\beta) \tag{2}$$

Preprints (www.preprints.org) | NOT PEER-REVIEWED | Posted: 25 September 2023 doi:10.20944/preprints202309.1650.v1

where q is the gravity load per element volume of the supporting suspension cable or transmission line, σ_0 is the horizontal stress of the suspension cable, β is the angle of elevation difference, and $\tan\beta = h/l$, where h is h_s or h_c and l is the corresponding l_s or l_c.

2.3. The mechanical characteristics of TC-PTS

In TC-PTS, the supporting suspension cables and transmission lines are mainly subjected to tension, and to a lesser extent, they will also be subjected to bending and torsional moments. It is reasonable to neglect the bending and torsional capacities in wind vibration response analysis without considering torsion [12]. Therefore, in the TC-PTS wind vibration analysis, the supporting suspension cables and transmission lines were primarily considered for the axial tensile capacity.

3. Nonlinear finite element analytical model of wind-induced vibration and fatigue damage assessment for TC-PTS

3.1. Element stiffness matrix for supporting suspension cables and transmission lines

According to the mechanical characteristics of the TC-PTS, its supporting suspension and transmission line wind vibration are large deformation and small strain problems. Combined with the force characteristics of this power transmission structure, the finite element model shown in Figure 3 can be established using a 3D truss element by considering geometric nonlinear effects. Generally, the element stiffness matrix can be established using both the local and global coordinate systems. Compared with the stiffness matrix established in the local coordinate system [11,13,14], the element stiffness matrix in the global coordinate system [15–17] can be directly grouped into the system stiffness matrix. It can be directly grouped into a system stiffness matrix to effectively avoid the coordinate conversion process. For the three-dimensional truss element in the global coordinate system, the stiffness matrices are mostly derived using the principle of virtual work [15] and by deriving the truss ends [17]. However, the virtual work principle requires multiple integrals, and often results in implicit stiffness matrices that are difficult to apply directly, whereas the truss end strives for derivatives that require more complicated vector operations. Therefore, this study simplifies the operation through the relationship between the elastic energy of the 3D truss element and its deformation, and derives the explicit stiffness matrix of the 3D truss element under the global coordinate system.

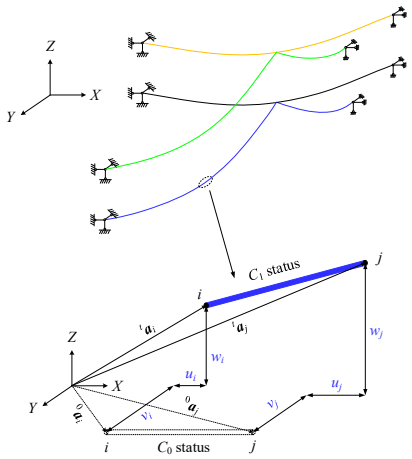

Figure 3. Simplified finite element model and node displacements.

In Figure 3, the physical quantities at the initial moment (C_0 state) are known quantities, and the node vectors at both ends of the element in the global coordinate system are

Preprints (www.preprints.org) | NOT PEER-REVIEWED | Posted: 25 September 2023 doi:10.20944/preprints202309.1650.v1

$$\begin{cases} {}^0\boldsymbol{a}_i = \{x_i \quad y_i \quad z_i\}^T \\ {}^0\boldsymbol{a}_j = \{x_j \quad y_j \quad z_j\}^T \end{cases} \tag{3}$$

The principle of vector subtraction is then used to obtain the element vectors of the truss element in the global coordinate system.

$${}^0\boldsymbol{a}_e = {}^0\boldsymbol{a}_j - {}^0\boldsymbol{a}_i = \{x_j - x_i \quad y_j - y_i \quad z_j - z_i\}^T \tag{4}$$

After time t, the truss element undergoes a displacement deformation movement to C_1 state, and the displacement vector of the nodes at both ends of the element under the global coordinate system is

$$\begin{cases} \boldsymbol{u}_i = \{u_i \quad v_i \quad w_i\}^T \\ \boldsymbol{u}_j = \{u_j \quad v_j \quad w_j\}^T \end{cases} \tag{5}$$

From Eq. (3) and (5), the node vectors at both ends of the element in the global coordinate system are

$$\begin{cases} {}^t\boldsymbol{a}_i = {}^0\boldsymbol{a}_i + \boldsymbol{u}_i \\ {}^t\boldsymbol{a}_j = {}^0\boldsymbol{a}_j + \boldsymbol{u}_j \end{cases} \tag{6}$$

Therefore, the element vector of the truss element at time t is

$${}^t\boldsymbol{a}_e = {}^0\boldsymbol{a}_e + \boldsymbol{u}_j - \boldsymbol{u}_i \tag{7}$$

According to the node displacement vector, the element displacement vector can be expressed as

$$\boldsymbol{u}_e = \{u_i \quad v_i \quad w_i \quad u_j \quad v_j \quad w_j\}^T \tag{8}$$

Eq. (7) can be further expressed as Eq. (8) as:

$${}^t\boldsymbol{a}_e = {}^0\boldsymbol{a}_e + \left[-\boldsymbol{I}_{3\times3} \quad \boldsymbol{I}_{3\times3}\right]\boldsymbol{u}_e \tag{9}$$

where $\boldsymbol{I}_{3\times3}$ is the 3rd order element matrix.

At C_0 state, the truss element in the state has no strain and its element length is

$${}^0l = \left|{}^0\boldsymbol{a}_e\right| = \sqrt{{}^0\boldsymbol{a}_e^T\,{}^0\boldsymbol{a}_e} \tag{10}$$

At C_1 state, the length of the truss element in the state is:

$${}^t l = \left|{}^t\boldsymbol{a}_e\right| = \sqrt{{}^t\boldsymbol{a}_e^T\,{}^t\boldsymbol{a}_e} \tag{11}$$

At this point, the strain in the truss element is:

$${}^t\varepsilon = ({}^t l - {}^0 l) / {}^0 l \tag{12}$$

The truss element elastic energy ${}^tU$ at time t can be calculated using equation (13):

$${}^tU = \int_V \int_0^{{}^t\varepsilon} \sigma(\varepsilon) d\varepsilon dV \tag{13}$$

where: $\sigma(\varepsilon)$ is the stress of the truss element, and the relationship between stress and strain in the linear elastic range is: $\sigma(\varepsilon) = E\varepsilon$, E is the Young's modulus, V is the element volume, when the cross-section area of the truss element is a constant value of A, Eq. (13) can be further expressed as

Preprints (www.preprints.org) | NOT PEER-REVIEWED | Posted: 25 September 2023 doi:10.20944/preprints202309.1650.v1

$$ {}^{t}U = \frac{1}{2} EA\, {}^{0}l\, {}^{t}\varepsilon^{2} \tag{14} $$

The element tangent stiffness matrix at time t in the global coordinate system can be calculated using the Hessian matrix as follows:

$$ {}^{t}\boldsymbol{K}_{e} = \frac{\partial^{2}\, {}^{t}U}{\partial\, {}^{t}\boldsymbol{u}_{e}\, \partial\, {}^{t}\boldsymbol{u}_{e}^{T}} \tag{15} $$

The final result of the element tangent stiffness matrix at time t is:

$$ {}^{t}\boldsymbol{K}_{e} = \frac{EA\, {}^{t}\varepsilon}{{}^{t}l} \begin{bmatrix} \boldsymbol{I}_{3\times3} & -\boldsymbol{I}_{3\times3} \\ -\boldsymbol{I}_{3\times3} & \boldsymbol{I}_{3\times3} \end{bmatrix} + \frac{EA}{{}^{t}l^{3}} \begin{bmatrix} {}^{t}\boldsymbol{a}_{e}\, {}^{t}\boldsymbol{a}_{e}^{T} & -{}^{t}\boldsymbol{a}_{e}\, {}^{t}\boldsymbol{a}_{e}^{T} \\ -{}^{t}\boldsymbol{a}_{e}\, {}^{t}\boldsymbol{a}_{e}^{T} & {}^{t}\boldsymbol{a}_{e}\, {}^{t}\boldsymbol{a}_{e}^{T} \end{bmatrix} \tag{16} $$

The element tangent stiffness matrix ${}^{t}\boldsymbol{K}_{e}$ shown in Eq. (16) is derived by introducing only the linear elasticity assumption and not the small deformation assumption, which is an exact tangent stiffness matrix at any displacement. Therefore, it is applicable to the case of arbitrarily large deformations and small strains.

3.2. Element mass matrix and damping matrix

The TC-PTS finite element model mass matrix is constructed using a consistent mass matrix with an element-consistent mass matrix as follows:

$$ \boldsymbol{M}_{e} = \frac{{}^{0}l\rho A}{6} \begin{bmatrix} 2\boldsymbol{I}_{3\times3} & \boldsymbol{I}_{3\times3} \\ \boldsymbol{I}_{3\times3} & 2\boldsymbol{I}_{3\times3} \end{bmatrix} \tag{17} $$

where ${}^{0}l$ is the initial length of the element, ρ is the mass density of the element, respectively.

The element damping matrix is constructed using Rayleigh damping:

$$ {}^{t}\boldsymbol{C}_{e} = \alpha_{v}\boldsymbol{M}_{e} + \beta_{v}\, {}^{t}\boldsymbol{K}_{e} \tag{18} $$

where α_v and β_v are the Rayleigh damping constants calculated using Eq. (19) and Eq. (20):

$$ \alpha_{v} = 2\xi_{k1}\omega_{k1}\omega_{k2} / (\omega_{k1} + \omega_{k2}) \tag{19} $$

$$ \beta_{v} = 2(\xi_{k2}\omega_{k2} - \xi_{k1}\omega_{k1}) / (\omega_{k1}^{2} + \omega_{k2}^{2}) \tag{20} $$

where ω_{k1} and ω_{k2} are the intrinsic frequencies of the k1st and k2nd order modes, respectively; ξ_{k1} and ξ_{k2} is the damping ratio corresponding to the k1st and k2nd order modes, respectively. This can be considered as $\beta_v = 0$ [18]. In which case, ${}^{t}\boldsymbol{C}_{e}$ is not affected by the change in structural displacement, namely, $\boldsymbol{C}_{e}$.

3.3. Equivalent nodal load vector

The primary loads to which the TC-PTS was subjected were gravity and wind. The static and dynamic displacements of this power transmission structure are based on the gravity load equilibrium position. Therefore, when calculating the structural equivalent nodal load vector, the gravity load is equivalent to the internal nodal load vector at the reference position. For the truss elements of the TC-PTS finite element model, the wind load per unit length was calculated using equation (21):

$$ F_{D} = \frac{1}{2}\rho_{air} V_{z}^{2} C_{D} A_{m} \tag{21} $$

where ρ_{air} is the air density, V_z is the wind speed, C_D is the drag coefficient, A_m is the windward projected area per unit length of the truss element, for supporting suspension cables: $A_m = d\cos\theta$, for

Preprints (www.preprints.org) | NOT PEER-REVIEWED | Posted: 25 September 2023 doi:10.20944/preprints202309.1650.v1

transmission lines: $A_m = d\sin\theta$, d is the diameter of the truss element, and θ is the angle of the wind direction (shown in Figure 4).

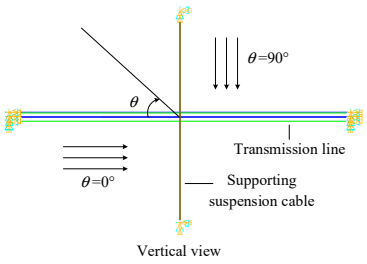

Figure 4. Schematic diagram of wind direction angle θ.

V_z can be calculated using equation (22):

$$V_z = V_s(z) + V(t) \tag{22}$$

where $V_s(z)$ is the average wind speed, $V(t)$ is the pulsating wind speed.

The pulsating wind speed $V(t)$ is generated by the harmonic synthesis method [19]. The average wind speed $V_s(z)$ can be calculated from the exponential law according to equation (23):

$$V_s(z) = (z/10)^{\alpha} V_{10} \tag{23}$$

Where V_{10} is the reference average wind speed at the height of 10 m, z is the height, and α is the ground roughness coefficient. As TC-PTS is in the mountainous terrain, its ground roughness category can be considered as C. According to the "Code for Structural Loads of Buildings" [20], α is taken as 0.22.

The wind loads on the element are converted to element equivalent nodal loads, namely:

$${}^{t}\boldsymbol{F}_e = \frac{1}{2}\,{}^{t}l\begin{bmatrix} F_{ix} & F_{iy} & F_{iz} & F_{jx} & F_{jy} & F_{jz} \end{bmatrix}^T \tag{24}$$

where F_{ix} is the equivalent nodal load of the wind load in the X-direction at node i, and the rest are similar.

3.4. Establishment of the nonlinear dynamic equation

The mass matrix, stiffness matrix, damping matrix, and equivalent nodal load vectors of each element of the TC-PTS were assembled respectively, and nonlinear dynamic equations of the structure were established at the reference position based on the updated Lagrange column equation:

$$\boldsymbol{M}\,{}^{t+\Delta t}\ddot{\boldsymbol{u}} + \boldsymbol{C}\,{}^{t+\Delta t}\dot{\boldsymbol{u}} + {}^{t+\Delta t}\boldsymbol{Q} - {}^{0}\boldsymbol{Q} = {}^{t+\Delta t}\boldsymbol{F} \tag{25}$$

where ${}^{t+\Delta t}\ddot{\boldsymbol{u}}$ and ${}^{t+\Delta t}\dot{\boldsymbol{u}}$ are the acceleration and velocity vectors of the structure at time $t+\Delta t$, $\boldsymbol{M}$ and $\boldsymbol{C}$ are the mass and damping matrix of the structure. ${}^{t+\Delta t}\boldsymbol{Q}$ and ${}^{0}\boldsymbol{Q}$ are the internal load vectors, that is, the internal nodal load vectors at time $t+\Delta t$ and the reference position, respectively. In addition, ${}^{t+\Delta t}\boldsymbol{F}$ is the equivalent nodal load vector of the structure at time $t+\Delta t$.

When Δt is sufficiently small, the displacement increment of the structure within a time step is small, and ${}^{t+\Delta t}\boldsymbol{Q}$ and ${}^{t}\boldsymbol{K}$ can be approximated using the following linear relationship:

$${}^{t+\Delta t}\boldsymbol{Q} = {}^{t}\boldsymbol{Q} + {}^{t}\boldsymbol{K}\boldsymbol{u} \tag{26}$$

where ${}^{t}\boldsymbol{Q}$ is the internal nodal load vector at time t, ${}^{t}\boldsymbol{K}$ is the stiffness matrix of the structure at time t, and $\boldsymbol{u}$ is the displacement increment within Δt, that is $\boldsymbol{u} = {}^{t+\Delta t}\boldsymbol{u} - {}^{t}\boldsymbol{u}$.

Combining Eq. (25) and Eq. (26), the nonlinear dynamic equations in the form of displacement increments are obtained.

Preprints (www.preprints.org) | NOT PEER-REVIEWED | Posted: 25 September 2023 doi:10.20944/preprints202309.1650.v1

$$\boldsymbol{M}\,{}^{t+\Delta t}\ddot{\boldsymbol{u}} + \boldsymbol{C}\,{}^{t+\Delta t}\dot{\boldsymbol{u}} + {}^{t}\boldsymbol{K}\boldsymbol{u} = {}^{t+\Delta t}\boldsymbol{F} - [{}^{t}\boldsymbol{Q} - {}^{0}\boldsymbol{Q}] \tag{27}$$

3.5. Solution of the nonlinear dynamical equation

The Newmark-β method is used to solve the nonlinear finite element equations shown in Eq. (27). Because Eq. (26) is a linear approximation, the displacement increment of the solution produces a large error accumulation as the time step increases. Therefore, to improve the accuracy of the solution and avoid the accumulation of numerical instability within each time step, the Newton–Raphson iterative method was used in this study for balanced iterative calculation. The solution process is summarized as follows.

Step 1: Calculate the individual element characterization matrices ${}^{0}\boldsymbol{K}_{e}$, $\boldsymbol{M}_{e}$, and $\boldsymbol{C}_{e}$ based on the initial shape and strain of the element, and then assemble them to obtain the characterization matrices ${}^{0}\boldsymbol{K}$, $\boldsymbol{M}$, and $\boldsymbol{C}$ f the structure.

Step 2: Apply the initial equivalent nodal load ${}^{0}\boldsymbol{F}$, and then calculate ${}^{0}\ddot{\boldsymbol{u}}$ from the initial conditions ${}^{0}\boldsymbol{u}$ and ${}^{0}\dot{\boldsymbol{u}}$:

$${}^{0}\ddot{\boldsymbol{u}} = \boldsymbol{M}^{-1}[{}^{0}\boldsymbol{F} - \boldsymbol{C}\,{}^{0}\dot{\boldsymbol{u}} - {}^{0}\boldsymbol{K}\,{}^{0}\boldsymbol{u}]$$

Step 3: Select the time step Δt and calculate the integration constant [21] using the known physical quantities at time t. The effective stiffness matrix was calculated before performing the iterations of ${}^{t}\hat{\boldsymbol{K}}^{(0)}$:

$${}^{t}\hat{\boldsymbol{K}}^{(0)} = {}^{t}\boldsymbol{K} + c_0\boldsymbol{M} + c_1\boldsymbol{C}$$

Step 4: Perform Newton–Raphson iterations. Calculate the effective load vector ${}^{t+\Delta t}\hat{\boldsymbol{F}}$ at time $t+\Delta t$:

$${}^{t+\Delta t}\hat{\boldsymbol{F}} = {}^{t+\Delta t}\boldsymbol{F} + \boldsymbol{M}[c_0\,{}^{t}\boldsymbol{u} + c_2\,{}^{t}\dot{\boldsymbol{u}} + c_3\,{}^{t}\ddot{\boldsymbol{u}}] + \boldsymbol{C}[c_1\,{}^{t}\boldsymbol{u} + c_4\,{}^{t}\dot{\boldsymbol{u}} + c_5\,{}^{t}\ddot{\boldsymbol{u}}]$$

From this, calculate the unbalanced force vector for the first iteration ${}^{t+\Delta t}\hat{\boldsymbol{F}}^{(0)}$:

$${}^{t+\Delta t}\hat{\boldsymbol{F}}^{(0)} = {}^{t+\Delta t}\hat{\boldsymbol{F}} - [{}^{t}\boldsymbol{Q}^{(0)} - {}^{0}\boldsymbol{Q}] - [c_0\boldsymbol{M} + c_1\boldsymbol{C}][{}^{t+\Delta t}\boldsymbol{u}^{(0)} - {}^{t}\boldsymbol{u}]$$

where ${}^{t}\boldsymbol{Q}^{(0)}$ is the internal nodal load vector before the first iteration, and ${}^{t+\Delta t}\boldsymbol{u}^{(0)}$ is the displacement before the first iteration, namely, ${}^{t}\boldsymbol{u}$.

Solve for the displacement increment $\boldsymbol{u}^{(1)}$ after the first iteration at time $t+\Delta t$:

$$\boldsymbol{u}^{(1)} = [{}^{t}\hat{\boldsymbol{K}}^{(0)}]^{-1}[{}^{t+\Delta t}\hat{\boldsymbol{F}}^{(0)}]$$

Step 5: Update ${}^{t}\boldsymbol{K}^{(1)}$ and ${}^{t}\boldsymbol{Q}^{(1)}$ and update the effective stiffness matrix ${}^{t}\hat{\boldsymbol{K}}^{(1)}$ and the displacement before iteration ${}^{t+\Delta t}\boldsymbol{u}^{(1)}$:

$${}^{t+\Delta t}\boldsymbol{u}^{(1)} = {}^{t+\Delta t}\boldsymbol{u}^{(0)} + \boldsymbol{u}^{(1)}$$

and the unbalanced force vector ${}^{t+\Delta t}\hat{\boldsymbol{F}}^{(1)}$:

$${}^{t+\Delta t}\hat{\boldsymbol{F}}^{(1)} = {}^{t+\Delta t}\hat{\boldsymbol{F}} - [{}^{t}\boldsymbol{Q}^{(1)} - {}^{0}\boldsymbol{Q}] - [c_0\boldsymbol{M} + c_1\boldsymbol{C}][{}^{t+\Delta t}\boldsymbol{u}^{(1)} - {}^{t}\boldsymbol{u}]$$

and calculate the displacement increment after the second iteration $\boldsymbol{u}^{(2)}$:

$$\boldsymbol{u}^{(2)} = [{}^{t}\hat{\boldsymbol{K}}^{(1)}]^{-1}[{}^{t+\Delta t}\hat{\boldsymbol{F}}^{(1)}]$$

Step 6: Determine whether the L2 norm of the unbalanced force vector ${}^{t+\Delta t}\hat{\boldsymbol{F}}^{(1)}$ satisfies the convergence condition; if not, loop Step 5 until the convergence condition is satisfied; if so, end the

Preprints (www.preprints.org) | NOT PEER-REVIEWED | Posted: 25 September 2023 doi:10.20944/preprints202309.1650.v1

Newton–Raphson iteration to obtain the final nonlinear displacement ${}^{t+\Delta t}\boldsymbol{u}$ at time $t+\Delta t$, and then obtain the velocity ${}^{t+\Delta t}\dot{\boldsymbol{u}}$ and acceleration ${}^{t+\Delta t}\ddot{\boldsymbol{u}}$ at time $t+\Delta t$.

3.6. Wind-induced fatigue damage assessment of TC-PTS

Using the displacement time history and velocity time history obtained from the above TC-PTS wind vibration nonlinear finite element analysis model, the stress time history of each part of the TC-PTS can be derived. The rain-flow counting method was then used to process the stress time history and obtain the stress amplitude distribution statistically. Finally, the number of stress cycles in which fatigue damage occurs can be obtained using the *S*–*N* curve. The logarithmic form of the *S*–*N* curve is shown in Eq. (28):

$$\lg N = C - m\lg S \tag{28}$$

where N is the number of stress cycles in which fatigue damage occurs, C and m are the material fatigue parameters, and S is the stress amplitude.

The fatigue parameters for support suspension materials [22] were obtained from $C = 13.84$ and $m = 3.5$. The fatigue parameters of the transmission line materials [23] are available for $N \le 2\times10^7$, $C = 13.27$, and $m = 5$, as well as for $N > 2\times10^7$, $C = 14.40$, and $m = 5.95$.

According to Miner's linear fatigue cumulative damage criterion, the wind vibration fatigue damage of each part of the TC-PTS is as follows:

$$D = \sum_{i=1}^{k} n_i / N_i \tag{29}$$

where D is the total fatigue damage value. When D = 1, fatigue damage occurs, k is the total number of stress amplitudes, n_i is the number of times the i^{th} stress amplitude occurs, and N_i is the number of stress cycles corresponding to the i^{th} stress amplitude where fatigue damage occurs.

In addition, wind vibration fatigue damage analysis of the supported suspension cables and transmission lines must consider the effect of the average stress. The Goodman model is often used to correct for the effect of the nonzero average stress S_m, namely:

$$S = S_0(1 - S_m / S_t) \tag{30}$$

where S is the actual stress amplitude, S_0 is the equivalent stress amplitude at zero average stress, S_m is the average stress, and S_t is the tensile strength of a material.

4. Example analysis

4.1. Example description

In this study, a two-span TC-PTS, as shown in Figure 5, was considered as the research object for wind vibration response analysis and fatigue damage assessment. In this study, the wind speed time duration was taken as 600 s, and the structural parameters of the two-span TC-PTS were l_s = 1000 m, l_c = 800 m, h_{wg} = 20 m, h_s = 0 m, and h_c = 0 m, respectively, and the endpoints of the supporting-conductor suspension cables were considered to be fixed at a height of 300 m. All the calculations required for the analysis in this study were performed on a computer with an Intel i5-9400F CPU and 32 GB of RAM.

Preprints (www.preprints.org) | NOT PEER-REVIEWED | Posted: 25 September 2023 doi:10.20944/preprints202309.1650.v1

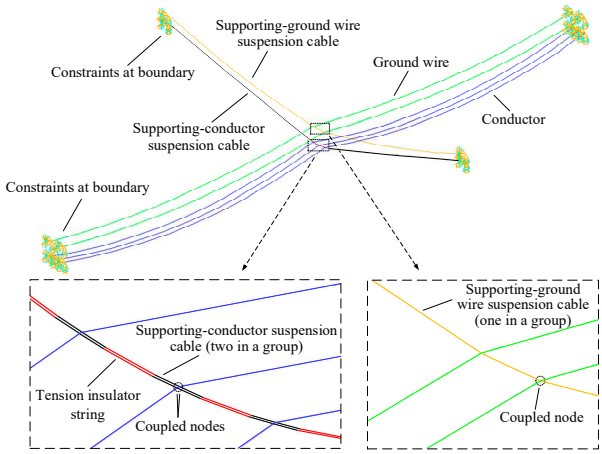

Figure 5. A two-span tension cable-supported power transmission structure.

Using the proposed model, the first five orders of natural frequency and the first three orders of the vibration mode of this power transmission structure can be calculated, as shown in Table 1 and Figure 6, respectively. The results of the frequency analysis in Table 1 show that the first five orders of intrinsic frequencies of the supporting-conductor part are 77.89%, 78.65%, 78.28%, 78.30%, and 78.30% of the corresponding values of the supporting-ground wire part. The lower-order natural frequency of the supporting-conductor part was lower than that of the supporting-ground wire part. As shown in Figure 6, for the supporting-conductor part, the first-, second-, and third-order vibration modes were antisymmetric vertical bending, symmetric lateral bending, and antisymmetric lateral bending, respectively.

Table 1. First five orders natural frequency of TC-PTS.

Parts	Frequency order	Proposed model/(Hz)	ANSYS/(Hz)	Relative error/(%)
The supporting-conductor part	first order	0.08063176	0.08063257	-0.001000
	second order	0.08174143	0.08174136	0.000086
	third order	0.08186433	0.08186437	-0.000053
	fourth order	0.08188066	0.08188070	-0.000057
	fifth order	0.08188298	0.08188303	-0.000058
The supporting-ground wire part	first order	0.10351429	0.10351425	0.000046
	second order	0.10393417	0.10393408	0.000087
	third order	0.10457513	0.10457513	0.000000
	fourth order	0.10457779	0.10457779	0.000000
	fifth order	0.10457779	0.10457779	0.000000

Preprints (www.preprints.org) | NOT PEER-REVIEWED | Posted: 25 September 2023 doi:10.20944/preprints202309.1650.v1

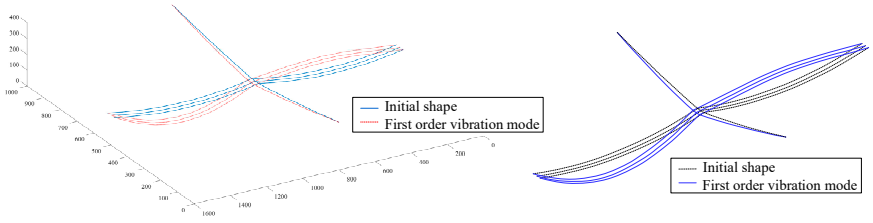

(**a**)

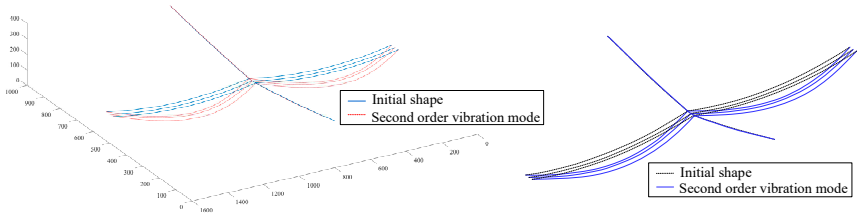

(**b**)

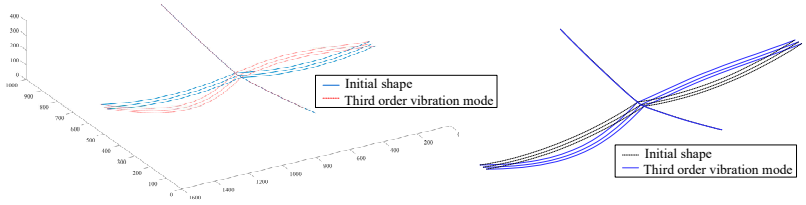

(**c**)

Figure 6. First three orders mode of vibration of the supporting-conductor part obtained by the proposed model (left) and ANSYS (right). (**a**) First order vibration mode; (**b**) Second order vibration mode; (**c**) Third order vibration mode.

To verify the correctness and calculation accuracy of the proposed model, ANSYS was used to perform a modal analysis, and the results of the two calculations were compared. In the ANSYS model, the supporting suspension and transmission line were simulated using the Link180 element, and the structural parameters, boundary conditions, and other parameters were consistent with those of the model in this study. The ANSYS calculation results are also given in Table 1 and Figure 6, respectively, and it can be seen that the maximum absolute value of the relative error of the frequency results of the proposed model is 0.001%, which is a better accuracy, and vibration modes are also consistent.

4.2. Wind-induced vibration response of TC-PTS

4.2.1. Time history analysis of TC-PTS wind-induced vibration response

The time history analysis of wind-induced vibration response of TC-PTS was performed by considering the working conditions of the wind speed $V_{10}=15\text{m/s}$ and wind direction angle $\theta=90^{\circ}$. The mean square error (σ) of lateral displacement at each location along the conductor length is shown in Figure 7, and it can be seen that the mean square error of lateral displacement in the center of the conductor is the largest, which is 2.34 m, indicating that the location in the center of the conductor is more significantly affected by wind load, and the variance values of lateral displacement in the remaining locations are roughly symmetrical along the location in the center of the conductor. The lateral displacement time histories at the center of the conductor are shown in Figure 8, and the average and maximum values of the lateral displacement time histories in Figure 8 are listed in Table 2. The results in Table 2 and Figure 8 show that the average values of lateral displacement in the

Preprints (www.preprints.org) | NOT PEER-REVIEWED | Posted: 25 September 2023 doi:10.20944/preprints202309.1650.v1

conductor under wind load in this condition is 23.33 m, and its maximum value is 29.70 m, the lateral displacement is distributed from the minimum value of 16 m to the maximum value of 29.70 m, with a large variation.

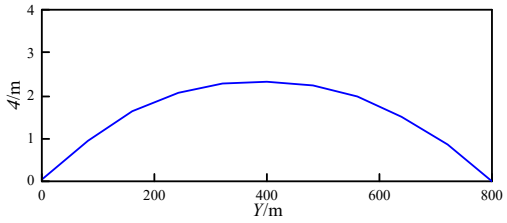

Figure 7. Mean square deviation of lateral displacement at each position of a single span conductor.

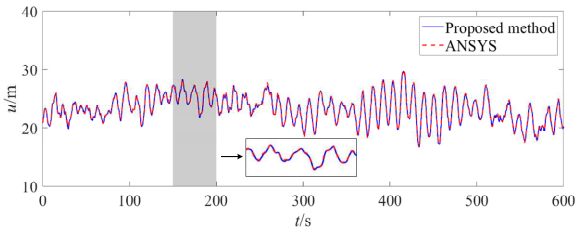

Figure 8. The lateral displacement time history of the conductor midpoint.

Similarly, the time history of the midpoint displacement of the conductor computed by ANSYS are plotted in Figure 8 and Table 2, whereas the computational efficiency of the proposed model is listed in Table 3. From Figure 8 and Table 2, it can be observed that the relative errors of the mean and maximum values of the lateral displacement time history obtained by the proposed model were 0.13% and 0.83%, respectively, and its accuracy was high. Simultaneously, the lateral displacement time history curves obtained by the proposed model have a consistent trend with the ANSYS results, which have a high degree of agreement. The results in Table 3 show that the computation time required by ANSYS to analyze the lateral displacement in the conductor was 35.88 min, whereas the computation time of the proposed model was 1.50 min, and its computational cost was only 4.19% of the former. Therefore, the proposed model can be applied to the wind-induced vibration nonlinear finite element analysis for TC-PTS more efficiently.

Table 2. Average and maximum values obtained by the proposed model and ANSYS.

Terms	Average values	Maximum values
Proposed model	23.33m	29.70m
ANSYS	23.36m	29.95m
Relative error/(%)	0.13	0.83

Table 3. Calculation efficiency obtained by the proposed model and ANSYS.

Terms	Computing time/min	Calculation efficiency/%
Proposed model	1.50	4.19
ANSYS	35.88	-

4.2.2. Effect of different wind direction angles on TC-PTS wind-induced vibration response

In this section, the influence of different wind direction angles (θ taken as 0°, 45°, 60°, and 90°) on the maximum lateral displacement of the transmission line and the maximum tension of the supporting suspension cables of TC-PTS at $V_{10} = 20\text{m/s}$ are investigated. The variation in the maximum lateral displacement of the transmission line and the maximum tension of the supporting suspension cable with the wind direction angle θ is shown in Figure 9. In Figure 9a, it can be seen

Preprints (www.preprints.org) | NOT PEER-REVIEWED | Posted: 25 September 2023 doi:10.20944/preprints202309.1650.v1

that the maximum lateral displacement of the transmission line increases with the increase in θ, and initially, it tends to be faster and slower subsequently. In Figure 9b, the maximum tension of the supporting suspension cable increases with the increase in θ. The change in the incremental magnitude of the maximum lateral displacement of the transmission line was also owing to the stress-stiffening effect of the structure. Considering the conductor as an example, the maximum lateral displacements of the conductor are 0.0071, 21.15, 28.12, and 32.96 m for wind direction angles of 0°, 45°, 60°, and 90°, respectively, and the most unfavorable wind direction angle for the maximum lateral displacement of the transmission line is 90°. The maximum tension of the supporting suspension cables increased with the wind direction angle because the downwind projected area of the transmission line was larger than that of the supporting suspension cables. As the wind direction angle increased, the global wind load on the structure increased. Therefore, the wind direction angle had a more significant effect on both the lateral displacement of the transmission line and the tension of the supporting suspension cables and the most unfavorable wind direction angle for the two-span TC-PTS was 90°.

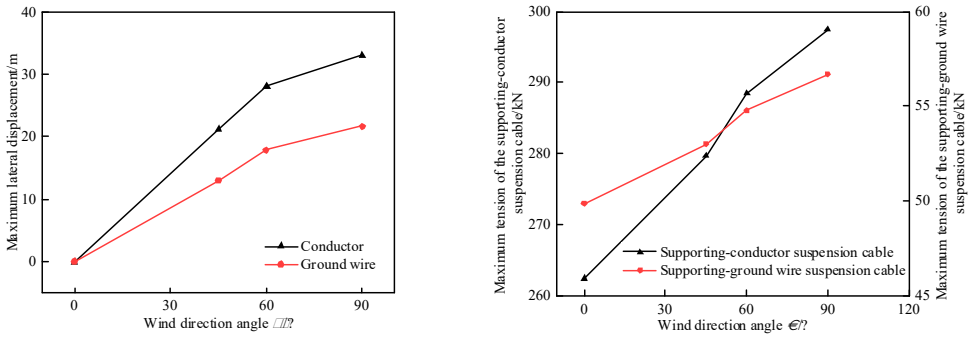

(**a**) (**b**)

Figure 9. The influence of wind direction angle θ. (**a**) Maximum lateral displacement of the transmission line; (**b**) Maximum tension of the supporting suspension cable.

4.2.3. Effect of different wind speeds on the wind-induced vibration response of TC-PTS

Based on the conclusions of the above analysis, this section examines the effect of the change of wind speed V_{10} on the maximum lateral displacement of the transmission line and the maximum tension of the supporting suspension cables under the most unfavorable wind direction angle of 90° working condition. The variation of the maximum lateral displacement of the transmission line and the maximum tension of the supporting suspension cable with the wind speed V_{10} at $\theta = 90^{\circ}$ is shown in Figure 10. In Figure 10a, it can be seen that the maximum lateral displacement of the transmission line increases with the increase of V_{10}, and the magnitude of the increase tends to be faster initially which becomes slow subsequently. This phenomenon is more obvious on the conductor. In Figure 10b, the maximum tension of the supporting suspension cables increases with the increase in V_{10} all the time. The change of the maximum lateral displacement increment of the transmission line is due to the stress stiffening effect of the structure, according to Eq. (16), the element tangent stiffness increases with the increase in displacement, and the lateral stiffness of the structure also increases gradually with the increase in displacement. When the lateral stiffness is larger, the increase in lateral displacement of the transmission line will slow down.

Maximum lateral displacement of transmission line considering the maximum lateral displacement of conductor as an example, the wind speed is 5, 10, 15, 20, 25, and 30 m/s, and the maximum lateral displacement of conductor is 2.83, 11.03, 22.48, 32.96, 40.16, and 44.78 m, respectively. The wind speed is from 5 m/s, and every increase of 5 m/s, the maximum lateral displacement of conductor increases by 8.20, 11.45, 10.48, 7.21, and 4.62 m, respectively. Therefore, in the case of smaller wind speed, the increase in wind speed will be higher. The maximum lateral displacement of the conductor increases by 8.20, 11.45, 10.48, 7.21, and 4.62 m. Therefore, the increase in wind speed increases the maximum lateral displacement of the transmission line more

Preprints (www.preprints.org) | NOT PEER-REVIEWED | Posted: 25 September 2023 doi:10.20944/preprints202309.1650.v1

significantly when the wind speed is low, whereas the maximum lateral displacement of the transmission line is less affected by the wind speed when the wind speed is high. The change in the maximum tension of the supporting suspension cables is due to the fact that the suspension tension is required to balance the equivalent nodal loads, and the increase in wind speed increases the suspension tension all the time.

Maximum tension of supporting suspension cables taking the maximum tension of supporting-conductor suspension cable as an example, the wind speed starts from 5 m/s, and every increase of 5 m/s, the maximum tension of supporting-conductor suspension cable increases by 6.59, 11.05, 15.62, 20.38, and 25.47 kN, respectively, and the increment of the maximum tension is approximately linearly related to the wind speed, the maximum tension and the quadratic of the wind speed are approximately linearly correlated, at the wind speed is small, the maximum tension of the supporting suspension cable is less affected by wind speed, while in the wind speed is larger, the maximum tension of the supporting suspension cable is more significantly affected by wind speed.

Therefore, at lower wind speeds V_{10}, the lateral displacement of the transmission line was more affected by the wind speed than the tension of the supporting suspension cable, and at higher wind speeds V_{10}, the tension of the supporting suspension cable was more notably affected by wind speeds than the lateral displacement of the transmission line.

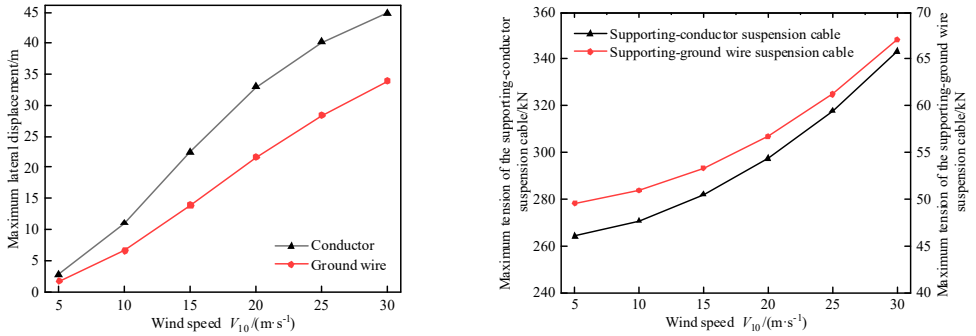

Figure 10. The influence of wind speed V_{10}. (**a**) Maximum lateral displacement of the transmission line; (**b**) Maximum tension of the supporting suspension cable.

4.3. Wind-induced fatigue damage of TC-PTS

4.3.1. Wind-induced fatigue damage assessment of TC-PTS

To comprehensively analyze the wind vibration fatigue damage condition of the two-span TC-PTS, the ends and midpoint of the supporting-conductor suspension cable and conductor were selected as fatigue analysis parts. The ends and midpoint of the supporting-conductor suspension cable and conductor are points A, B, C, and D, respectively. The wind-induced fatigue damage of each fatigue analysis part of the two-span TC-PTS was calculated by considering the working conditions of wind speed $V_{10}=15\text{m/s}$ and wind direction angle $\theta=90^{\circ}$ as examples. The stress time history of each fatigue analysis part is shown in Figure 11, and the corresponding mean stress, mean square deviation, and fatigue damage are listed in Table 4. It can be observed that, compared with point A, the stress mean value of point B is larger, but the mean square deviation is smaller, and its fatigue damage is smaller because the stress amplitude has a more significant effect on the fatigue damage value: the larger the mean square deviation, the more frequently the high stress amplitude occurs, and the more serious the corresponding fatigue damage. The mean stress value and mean square deviation of point C were greater than those of point D, and the fatigue damage value was also greater.

Preprints (www.preprints.org) | NOT PEER-REVIEWED | Posted: 25 September 2023 doi:10.20944/preprints202309.1650.v1

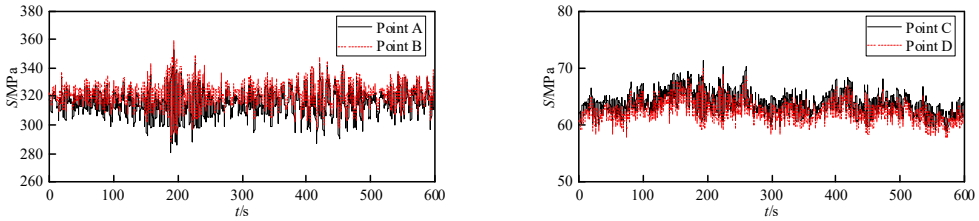

(a) (b)

Figure 11. Stress time history of each part. (**a**) The supporting-conductor suspension cable; (**b**) The conductor.

Table 4. Fatigue damage of each part.

Part	Mean value of stress/(MPa)	Mean square deviation of stress/(MPa)	Fatigue damage
Point A	315.04	9.12	9.70×10^{-11}
Point B	320.96	8.37	7.79×10^{-11}
Point C	63.70	1.87	1.41×10^{-12}
Point D	62.36	1.83	4.96×10^{-13}

4.3.2. Effect of different wind direction angles on wind-induced fatigue damage of TC-PTS

At $V_{10}=20\text{m/s}$, the influences of different wind direction angles θ on the fatigue damage of various parts of the TC-PTS are listed in Table 5. With a gradual increase in the wind direction angle, the wind load acting on the conductor is larger because of the coupling effect between the conductor and the supporting-conductor suspension cable, and the load borne by the supporting-conductor suspension cable also gradually increases. Therefore, the fatigue damage of each part increases, in the same working condition, the fatigue damage of the supporting-conductor suspension cable end (point A) is larger than that of the midpoint (point B), while the fatigue damage of the conductor end (point C) is smaller than that of the midpoint (point D). It is easy to see that among the wind direction angles, 90° wind direction angle has the most significant effect on the wind-induced fatigue damage of the TC-PTS.

Table 5. Fatigue damage of each part under different wind directions.

Case	Wind direction/(°)			
	0	45	60	90
Point A	2.91×10^{-12}	4.43×10^{-11}	2.72×10^{-10}	1.80×10^{-9}
Point B	3.30×10^{-12}	1.29×10^{-11}	1.43×10^{-10}	8.87×10^{-10}
Point C	2.01×10^{-14}	1.17×10^{-13}	1.33×10^{-12}	6.13×10^{-11}
Point D	1.50×10^{-14}	5.25×10^{-13}	9.28×10^{-12}	4.11×10^{-10}

4.3.3. Effect of different wind speeds on wind-induced fatigue damage of TC-PTS

Under the 90° wind direction angle condition, the effect of wind speed V_{10} change on the fatigue damage of each part of TC-PTS is shown in Table 6. As shown in the table, the wind-induced fatigue damage of each part increases with an increase in the wind speed V_{10}, and the fatigue damage at the end of the supporting-conductor suspension cable (point A) is larger than the fatigue damage of the midpoint (point B) under the same working conditions. With the gradual increase in wind speed V_{10}, the fatigue damage of all parts of the supporting-conductor suspension cable and conductor showed a tendency to increase faster and then slower. The fatigue damage of all parts of the supporting-conductor suspension cable increased gradually from to 10^{-16} to 10^{-8}, whereas the fatigue damage of all parts of the conductor increased gradually from to 10^{-25} to 10^{-7}. When the wind direction angle was 90°, the wind load per unit length of the conductor was greater than that of the supporting-conductor

 doi:10.20944/preprints202309.1650.v1

suspension cable, and the fatigue damage of each part of the conductor increased more than that of the supporting-conductor suspension cable.

Table 6. Fatigue damage of each part under different wind speeds.

Wind speed/(m·s^{-1})	Point A	Point B	Point C	Point D
5	1.40×10^{-15}	1.31×10^{-16}	1.14×10^{-24}	2.64×10^{-25}
10	2.87×10^{-12}	1.59×10^{-13}	5.13×10^{-18}	1.47×10^{-16}
15	9.70×10^{-11}	7.79×10^{-11}	1.41×10^{-12}	4.96×10^{-13}
20	1.80×10^{-9}	8.87×10^{-10}	6.13×10^{-11}	4.11×10^{-10}
25	7.72×10^{-9}	3.84×10^{-9}	1.59×10^{-8}	8.39×10^{-8}
30	5.81×10^{-8}	1.70×10^{-8}	8.03×10^{-7}	3.32×10^{-7}

5. Conclusions

The TC-PTS is a new class of power transmission structures suitable for mountainous terrain. A nonlinear finite element model of the wind-induced vibration for the TC-PTS was established using the nonlinear finite element method. Wind-induced vibration response analysis and fatigue damage assessment were carried out for a two-span TC-PTS, and the effect of wind speeds and wind direction angles on wind-induced vibration response and fatigue damage of the TC-PTS were discussed. The main conclusions are as follows:

(1) The comparison results show that the natural frequency and displacement time history calculated by the proposed model are highly accurate and can accurately calculate the structural dynamic characteristics and dynamic response. The proposed model also has high computational efficiency, and the computational cost of obtaining the dynamic response is only 4.19% of that of ANSYS.

(2) The low-order natural frequency of the supporting-conductor part was lower than that of the supporting-ground wire part; however, both values were still of the same order of magnitude. The first three order vibration modes of the supporting-conductor part were antisymmetric vertical bending, symmetric side bending, and antisymmetric side bending.

(3) For the mean wind load, at smaller wind speeds, the lateral displacement of the transmission line is more affected by wind speeds than the tension of the supporting suspension cable, at larger wind speeds, the tension of the supporting suspension cable is more notably affected by wind speeds than the lateral displacement of the transmission line.

(4) The fatigue damage value at the end of the supporting-conductor suspension cable was larger than that at the midpoint; however, they were approximately of the same order of magnitude. For the conductor, under the wind direction angle condition, the midpoint fatigue damage value is greater than the end fatigue damage value, whereas under the wind speed condition, the end and midpoint fatigue damage values have no obvious comparison.

(5) The wind-induced vibration response and fatigue damage of TC-PTS were significantly affected by the wind direction angle, and the results of the arithmetic analysis showed that the most unfavorable wind direction angle for TC-PTS was 90°.

Author Contributions: Conceptualization, Z.L. and T.W.; methodology, T.W.; software, J.L. and B.W.; validation, Z.L., T.W. and J.L.; formal analysis, T.W.; investigation, T.W., B.W. and J.Y.; resources, Z.L.; data curation, B.W.; writing—original draft preparation, J.L.; writing—review and editing, J.L. and B.W.; visualization, B.W.; supervision, T.W.; project administration, T.W.; funding acquisition, T.W. All authors have read and agreed to the published version of the manuscript.

Funding: The research presented in this paper was conducted with the support of the Special Support of Chongqing Postdoctoral Research Project (Grant No. 2022CQBSHBT3009) and the Special Postdoctoral Support Project of Chongqing Research Institute of HIT (Grant No.KY506023002).

Data Availability Statement: Not applicable.

Conflicts of Interest: The authors declare no conflict of interest.

References

1. Bai, H., Yi, T., Li, H., Ren, L. Multisensors on-site monitoring and characteristic analysis of UHV transmission tower. International Journal of Distributed Sensor Networks, 2012, 8(11): 545148.
2. Lou, W., Wu, D., Liu, M., Zhang, L., Bian, R. Properties of mountainous terrain wind field and their influence on wind-induced swing of transmission lines. China Civil Engineering Journal, 2018, 51(10): 46-55+77.
3. Irvine, H. Cable structure. New York: The MIT Press, 1981.
4. McClure, G., Lapointe, M. Modeling the structural dynamic response of overhead transmission lines. Computers and Structures, 2003, 81(8/9/10/11): 825-834.
5. Kempner, L., Smith, S. Cross-rope transmission tower-line dynamic analysis. Journal of Structural Engineering ASCE, 1984, 110(6): 1321-1335.
6. Tian, L, Pan, H., Ma, R., Dong, X. Seismic failure analysis and safety assessment of an extremely long-span transmission tower-line. Structural Engineering and Mechanics, 2019, 71(3): 305-315.
7. Fu, X., Li, H., Tian, L., Wang, J., Cheng, H. Fragility analysis of a transmission line subjected to wind loading. Journal of Performance of Constructed Facilities ASCE, 2019, 33(4): 1-11.
8. Yan, Z., Savory, E., Li, Z., Lin, W. Galloping of iced quad-conductors bundles based on curved beam theory. Journal of Sound and Vibration, 2014, 333(6): 1657-1670.
9. Yan, Z., Li, Z., Savory, E., Lin, W. Galloping of a single iced conductor based on curved-beam theory. Journal of wind engineering and industrial aerodynamics, 2013, 123: 77-87.
10. Chunming, W., Bin, M., Tingting, S. Research on the wind-induced vibration coefficient of transmission tower-line system. Physics Procedia, 2012, 24: 149-154.
11. Liu, X., Yan, B., Zhang, H., Zhou, S. Nonlinear numerical simulation method for galloping of iced conductor. Applied mathematics and mechanics, 2009, 30(4): 489-501.
12. Yan, Z., Huang, J., Li, Z. Finite element model of bundle lines based on 6-dof node. Engineering Mechanics, 2012, 29(8): 325-332.
13. Zhu, Z., Meguid, S. Analysis of three-dimensional locking-free curved beam element. International Journal of Computational Engineering Science, 2004, 5(03): 535-556.
14. Zhu, Z., Meguid, S. Vibration analysis of a new curved beam element. Journal of Sound and Vibration, 2008, 309(1-2): 86-95.
15. Chen, Z., Zeng, Q., Yan, Q. A UL formulation for internal force analysis of spatial frame structures with large displacement. China Civil Engineering Journal, 1992, 25(5): 34-43.
16. Shi, H., Salim, H. Geometric nonlinear static and dynamic analysis of guyed towers using fully nonlinear element formulations. Engineering Structures, 2015, 99: 492-501.
17. Liu, S. Accurate analysis method on the tangential stiffness matrix of pinned straight rod element. Chinese Journal of Computational Mechanics, 2014, 31(1): 48-53.
18. Desai, Y., Yu, P., Popplewell, N., Shah, A. Finite element modelling of transmission line galloping. Computers & structures, 1995, 57(3): 407-420.
19. Jakob, M. Wind field simulation. Probabilistic Engineering Mechanics, 1998, 13(4).
20. GB 50009-2012, Load code for the design of building structures. China Architecture & Building Press: Beijing, China, 2012.
21. Wang, X. Finite Element Method. Beijing: Tsinghua University Press, 2003.
22. Yan, L., Li, J., He, X. Effect of central clamps on fatigue damage of suspenders of suspension bridge under joint action of fluctuating wind and vehicle loads. Journal of Central South University (Science and Technology), 1-14.
23. Kong, D., Li, L., Long, X., Ye, Z. Parametric investigation on fatigue life of transmission line subjected to Aeolian vibration. Journal of Wuhan University of Technology, 2010, 32(10): 53-57.